JGR Atmospheres

RESEARCH ARTICLE
10.1029/2024JD042059

# Implementing Parameterizations of Sub-Pixel Terrain Long-Wave Radiative Effect for FY-4A/AGRI Infrared Data Assimilation Over Land Based on the Community Radiative Transfer Model

**Xin Li**[1], **Anning Huang**[2], **Mingjian Zeng**[1], **Yang Wu**[1], **Chunlei Gu**[2], **and Ning Wang**[3]

[1]Key Laboratory of Transportation Meteorology of China Meteorological Administration, Nanjing Joint Institute for Atmospheric Sciences, Nanjing, China, [2]School of Atmospheric Sciences, Nanjing University, Nanjing, China, [3]Jiangsu Climate Center, Nanjing, China

**Key Points:**

- Default Community Radiative Transfer Model (CRTM) leads to orography dependent simulation biases for FY-4A /AGRI over rugged areas
- A sub-pixel terrain long-wave radiative effect parameterization scheme is developed in CRTM for FY-4A/AGRI
- Considering the sub-pixel terrain long-wave radiative effect can clearly improve the accuracy of infrared simulation over complex terrain

**Correspondence to:**
A. Huang and M. Zeng,
anhuang@nju.edu.cn;
swordzmj@qq.com

**Citation:**
Li, X., Huang, A., Zeng, M., Wu, Y., Gu, C., & Wang, N. (2024). Implementing parameterizations of sub-pixel terrain, long-wave radiative effect for FY-4A/AGRI infrared data assimilation over land based on the community radiative transfer model. *Journal of Geophysical Research: Atmospheres*, *129*, e2024JD042059. https://doi.org/10.1029/2024JD042059

Received 24 JUL 2024
Accepted 15 NOV 2024

**Author Contributions:**

**Conceptualization:** Xin Li, Anning Huang, Chunlei Gu
**Data curation:** Xin Li, Mingjian Zeng, Yang Wu, Ning Wang
**Formal analysis:** Xin Li, Anning Huang, Yang Wu, Chunlei Gu
**Investigation:** Xin Li, Anning Huang, Mingjian Zeng, Yang Wu, Chunlei Gu
**Methodology:** Xin Li, Anning Huang, Chunlei Gu
**Project administration:** Mingjian Zeng
**Resources:** Mingjian Zeng
**Software:** Xin Li, Yang Wu, Ning Wang
**Supervision:** Mingjian Zeng
**Validation:** Xin Li, Yang Wu, Ning Wang
**Visualization:** Xin Li, Yang Wu, Chunlei Gu, Ning Wang
**Writing – original draft:** Xin Li



**Abstract** The sub-pixel terrain long-wave radiative effect (STLRE) plays an important role in the satellite surface-sensitive infrared brightness temperature (TB) simulation over rugged areas, however, it is absent in current radiative transfer models. This study incorporates a STLRE scheme in the Community Radiative Transfer Model (CRTM) for the FY-4A/Advanced Geosynchronous Radiation Imager (AGRI). The total surface downwelling long-wave radiance (SDLR) over rugged areas at sub-pixel is composed of the radiance from the overlying atmosphere under plane-parallel radiation condition and the radiance emitted from surrounding terrains, weighted by the sky view factor (SKV). Based on the homogenous assumption, a STLRE scheme is established through constructing terrain correction factors at AGRI pixel scale. The ExpCTL/ExpTOPO experiments with the CRTM adopting the plane-parallel scheme/STLRE scheme are conducted to evaluate the simulations of AGRI clear-sky TB over the rugged areas. Results show that considering the STLRE can significantly reduce the orography dependent simulation biases in the plane-parallel scheme. The reductions of biases for the AGRI channel 11–13 regionally averaged over the rugged areas are 64.2%, 72.7% and 67.6%, respectively. Stable correction performance is found at different times of the day. Meanwhile, the corrections of SDLR are more obvious in winter than in summer, and in barren condition than in the other land cover types. This is theoretically attributed to the land-air temperature difference and the land surface emissivity, respectively. This pilot study improves the observation operator for infrared TB data assimilation over complex terrain and exhibits broad promotion and application value.

**Plain Language Summary** Satellite observations are important for modern numerical weather predictions, but underutilized. Many valuable satellite observations near the surface are not used in numerical models, especially over complex terrain regions. The sub-pixel terrain long-wave radiative effect (STLRE) plays an important role in the satellite surface-sensitive infrared TB simulation over rugged areas, however, it is absent in current radiative transfer models. Consequently, the TB simulation by default CRTM exhibits orography dependent biases over rugged areas. This study focuses on improving the data assimilation ability for infrared observations influenced by complex terrains. We incorporate a STLRE scheme into CRTM and explore the potential benefits for FY-4A/AGRI TB simulation using the 1-year TB simulation samples over eastern China during 2022–2023. The new scheme considers the obstruction of atmospheric downwelling radiance by terrain and also the emissive radiance from surrounding terrains. More accurate TB simulations are produced for FY-4A/AGRI. The results of this study suggest a promising avenue for improving satellite data assimilation over complex terrain in the future.

## 1. Introduction

With the development of the new generations of geostationary meteorological satellite observation technology (Bessho et al., 2016; Schmit et al., 2017; Yang et al., 2016), satellite data assimilation (DA) plays an increasingly important role in numerical weather prediction. Atmospheric temperature, humidity and cloud variables can be notably improved by directly assimilating infrared brightness temperature (TB) in either global or regional models (Eyre et al., 2022; Hilton et al., 2012; Li & Liu, 2009; Otkin & Potthast, 2019; Sawada et al., 2019; Yin et al., 2021; Zhang et al., 2016; Zou et al., 2015). However, challenges of fully utilizing satellite data in numerical

models still remains, especially in the cloudy areas (Geer et al., 2019; Honda et al., 2018; Li et al., 2021; Okamoto et al., 2019; Zhang et al., 2021) and in the regions near surface over land (Dutta et al., 2016; Qin & Zou, 2019).

Satellite surface-sensitive channels are important for DA because they contain meaningful information of low-level atmospheric thermal information. In the past decades, researchers made efforts on improving the satellite DA over land through better describing the two key parameters (English, 2008), that is, land surface emissivity (LSE) and land surface temperature (LST), in the radiative transfer model (RTM) (Weng, 2007). To improve the consistency between the observed and simulated TB of surface-sensitive channels, several methods have been proposed to update the background LST with the help of either satellite retrievals (Guedj et al., 2011) or surface station observations (Li et al., 2023). Also, the LSE schemes or data sets have been developed to consider the dynamically varying characteristics, such as the University of Wisconsin-Madison High Spectral Resolution Emissivity (UW_HSRemis) (Borbas & Ruston, 2010) and the one-dimensional variational estimation of LSE for Infrared Atmospheric Sounding Interferometer (Pavelin & Candy, 2014).

However, another critical issue for satellite DA over land is the influence of terrain relief which has impacts on the radiative transfer process near the surface. Complex terrain areas are often closely related to the triggering of severe convective weather. Assimilating satellite TB properly in these areas is quite important but also full of challenges. In the traditional observation operator of satellite DA, such as the Community Radiative Transfer Model (CRTM) (Han et al., 2007), the radiative transfer near surface is based on the plane-parallel scheme, which ignores the impact of terrain undulation on the surface downwelling long-wave radiance (SDLR). This deficiency may cause inaccurate SDLR which results in simulated errors of top-of-atmosphere (TOA) radiance. Therefore, considering the terrain impact in RTM is indispensable before satellite TB can be assimilated over rugged areas.

Based on the mountain radiation theory (Proy et al., 1989), compared to plane surface, the topography can either reduce the radiation by obstructing surface downwelling long-wave radiation from atmosphere or increase it by the emission from the adjacent terrains (Feldman et al., 2022; Oliphant et al., 2003). Yan et al. (2016, 2020) revealed that ignoring the terrain long-wave radiative effect may result in the biases larger than $10^2$ W·m$^{-2}$ over highly rugged regions. The importance of including the terrain long-wave radiative effect over mountainous regions has already attracted attention in the developments of both the model radiation parameterizations and the satellite-based retrieval algorithms. On one hand, for the broadband long-wave radiation application, Zhang et al. (2006) introduced the 2-dimensional terrain long-wave radiative effect into a regional climate model which considers the terrain obstruction but neglects the radiation emitted from adjacent terrains. Furthermore, Gu et al. (2024) found a notable improvement of 4∼10% daily surface downwelling long-wave radiation flux simulation over the Tibetan Plateau after implementing the 3-dimensional sub-grid terrain long-wave radiative effect parameterization. On the other hand, for the long-wave radiance at a specific wavelength band, Zhu et al. (2021) introduced topographic effect in the RTM-based LST retrieval algorithm, leading to large improvements of LST in the rugged areas where the sky view factor (SKV) is smaller than 0.7. In other studies, the LST retrieval algorithms based on specific wavelengths were also developed with accounting for terrain geometry and adjacent effects (He & Tang, 2023; Xue et al., 2023). The success of these studies encourages the development of satellite DA over rugged areas.

To our best knowledge, few studies have considered the TLRE in the observation operator for DA purpose. Since the pixel scale of the advanced infrared imagers onboard geostationary satellites have reached kilometer level, how to describe the sub-pixel terrain long-wave radiative effect (STLRE) over rugged surface is a critical issue. Also, because the observation operators of satellite DA, that is, fast RTMs, require quick calculations, the incorporated the STLRE should be the parameterization approach with high computation efficiency. Fengyun (FY)-4A/Advanced Geosynchronous Radiation Imager (AGRI) is the first advanced imagers of China launched since 2016. The AGRI TB observation-minus-background (O-B) biases have been evaluated over ocean and land (Tang et al., 2021), and even all-sky conditions (Xu et al., 2021). This study aims at developing a modified observation operator based on CRTM that are suitable for AGRI DA over rugged areas. The new scheme is explored for the clear-sky surface-sensitive TB simulation focusing on the central and eastern regions of China, which will support the assimilation of AGRI TB around high-relief terrains with low SKV values in the future.

The other parts of the article are organized as follows: Section 2 describes the FY-4A/AGRI observations, the CRTM clear-sky TB simulation, the modified CRTM with the consideration of STLRE scheme and the experimental design. Section 3 discusses the numerical results of simulated AGRI TB accuracy over rugged surface. Conclusion and discussion are given in Section 4.

## 2. Data and Method

### 2.1. FY-4A/AGRI and CRTM Simulation

The first one in the new generations of geostationary meteorological satellites in China, FY-4A, is positioned at 104.7°E above the equator. The AGRI (Yang et al., 2016) has 14 channels with wavelengths ranging from 0.47 to 13.5 μm. The infrared channels include two short-wave infrared window channels at 3.75 μm (Channel 7 and 8); two water vapor channels centered at 6.25 and 7.1 μm (Channel 9 and 10), respectively; three long-wave infrared surface-sensitive channels at 8.6, 10.8 and 12 μm (Channel 11–13), respectively; and a low tropospheric $CO_2$ absorption channel at 13.5 μm (Channel 14). The AGRI provides a full disk scan at pixel resolution of 4 km every 15 min for the surface-sensitive channels 11–13 which are concerned in this study.

The Gridpoint Statistical Interpolation (GSI) version 3.6 is employed, in which the CRTM version 2.2.3 is the observation operator for satellite DA. The CRTM 2.2.3 is employed because it shows reliable performance on clear-sky surface-sensitive infrared TB simulation over land with the help of incorporating monthly varying emissivity atlas within its framework. An online simulation for AGRI clear-sky TBs over land is performed. The CRTM (Han et al., 2007) input parameters including three-dimensional variables of atmospheric temperature, water vapor and two-dimensional variables of surface wind speed, wind direction and 2-m air temperature are extracted from the Weather Research and Forecasting (WRF) regional forecasts. The LST and LSE are carefully selected to minimize the uncertainty on surface-sensitive radiance simulation (Zhuge et al., 2018).

Figure 1a shows an example of FY-4A/AGRI observed TB at 1800 UTC 29 January 2023. The surface variable of LST provided for CRTM simulation (Figure 1b) is obtained from the official FY-4A/AGRI LST product with 4-km horizontal resolutions (Dong et al., 2023). The monthly LSE data set from the UW_HSRemis (Seemann et al., 2008) with 0.05° × 0.05° resolution are bilinearly interpolated onto the AGRI pixels and convoluted to the AGRI spectral response functions. An external LSE module using this data set for CRTM simulation is then incorporated into the GSI. Figures 1c and 1d compares the UW_HSRemis LSE distributions in January and July. At 8.6 μm, focusing on the rugged areas, the LSE values of forests around the borders of Sichuan Basin (28°N ~ 32°N, 104°E ~ 107°E) are lower in winter (Figure 1c) than those in summer (Figure 1d). The monthly LSE data set can represent temporal variations of thermal emissions from the Earth surface. The official AGRI cloud mask product (Wang et al., 2019) is used to identify the clear-sky pixels for further evaluation.

### 2.2. Modified CRTM Considering STLRE for FY-4A/AGRI

To describe the sub-pixel topography within the AGRI pixels, the digital elevation model (DEM) data from the Shuttle Radar Topography Mission (SRTM) (Jarvis et al., 2008) with a horizontal resolution of 3″ (~90m) is used.

According to the mountain radiation theory, the total SDLR in the terrain areas is composed of the SDLR from atmosphere under the plane-parallel condition and the long-wave radiance emitted from the surrounding terrains (Figure 2a). Based on the isotropic assumptions (Adams et al., 2011; Sicart et al., 2006), the SDLR at sub-pixel scale (Duguay, 1995; Gu et al., 2024; Robledano et al., 2022) is given by

$$L^{\downarrow}_{t,i} = L^{\downarrow}_{p,i} \cdot SKV_i + L_{sur,i} \cdot (1 - SKV_i) \tag{1}$$

where $L^{\downarrow}_{t,i}$, $L^{\downarrow}_{p,i}$ and $L_{sur,i}$ are the total SDLR, the SDLR from the atmosphere calculated by the plane-parallel scheme and the received long-wave radiance emitted from surrounding terrains, respectively. The subscript $i$ stands for the sub-pixel index of DEM data. Jiao et al. (2019) suggested that the technique proposed by Dozier and Frew (1990) is a proper way to calculate the sky view factor utilizing DEM data. Therefore, the sub-pixel scale sky view factor $SKV_i$ which represents the non-shadowed proportion of hemisphere from the target point to the sky (Figure 2f) is given by:

$$SKV_i = \frac{1}{N}\sum_{k=1}^{N} \sin S_i \cdot \cos(AZ_k - AS_i) \cdot \left(\frac{\pi}{2} - E_{AZ_k} - \sin E_{AZ_k} \cdot \cos E_{AZ_k}\right) + \cos S_i \cdot \cos^2 E_{AZ_k} \tag{2}$$

where $AZ_k$ is the azimuth in the $k$th direction centered on the target point, $E_{AZ_k}$ is the maximum elevation (Figure 2c) in the $k$th direction. As shown in Figure 2b, $AS_i$ is the sub-pixel scale terrain slope aspect (Figure 2e),

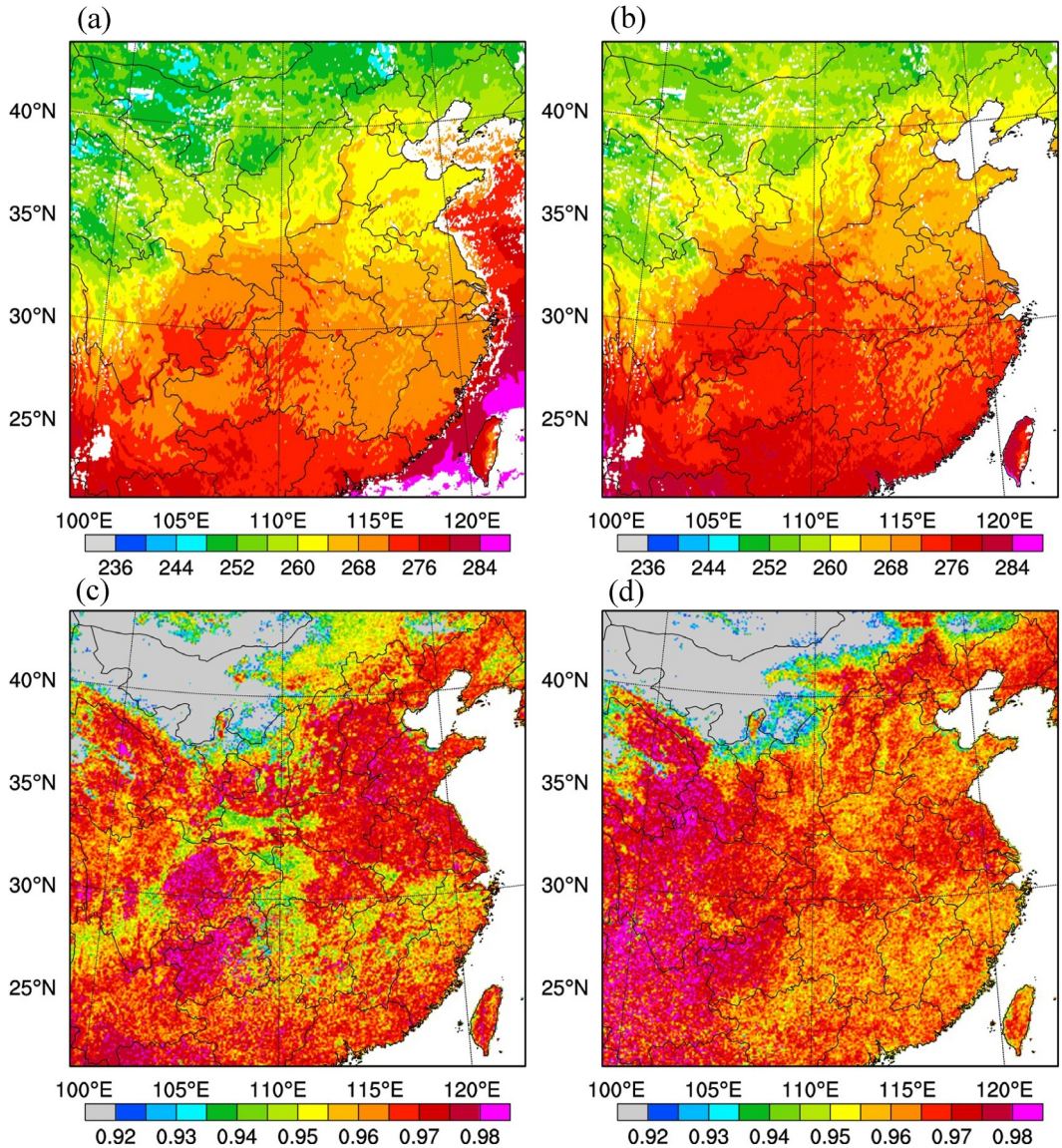


**Figure 1.** Spatial distributions of the (a) AGRI-observed channel 11 (8.6 μm) brightness temperature (shaded in color, unit: K) and the retrieved land surface temperature (shaded in color, unit: K) that is used in the CRTM simulation at 1800 UTC 29 January 2023. Spatial distributions of land surface emissivity in (c) January and (d) July for AGRI channel 11.

which is the angle between the normal of the inclined plane projected on the horizontal plane and the north direction. Both azimuth angle and terrain aspect slope angle vary from 0° to 360° clockwise with 0°, 90°, 180°, and 270° indicating the directions of north, east, south, and west, respectively. The sub-pixel scale terrain slope $S_i = \arctan\sqrt{\left(\frac{\partial z}{\partial x}\right)^2 + \left(\frac{\partial z}{\partial y}\right)^2}$ ranging from 0 to 90° (Figure 2d) is calculated based on the DEM terrain height $z$, horizontal coordinates $x$ and $y$ (Huang et al., 2022).

From the sub-pixel scale to the AGRI pixel scale, the SDLR over rugged terrains can be expressed as the aggregation of sub-pixel radiance,

$$L_t^{\downarrow} = \frac{1}{N}\sum_{i=1}^{N}\left(L_{t,i}^{\downarrow} \cdot \sec S_i\right) / \sum_{i=1}^{N} \sec S_i \tag{3}$$

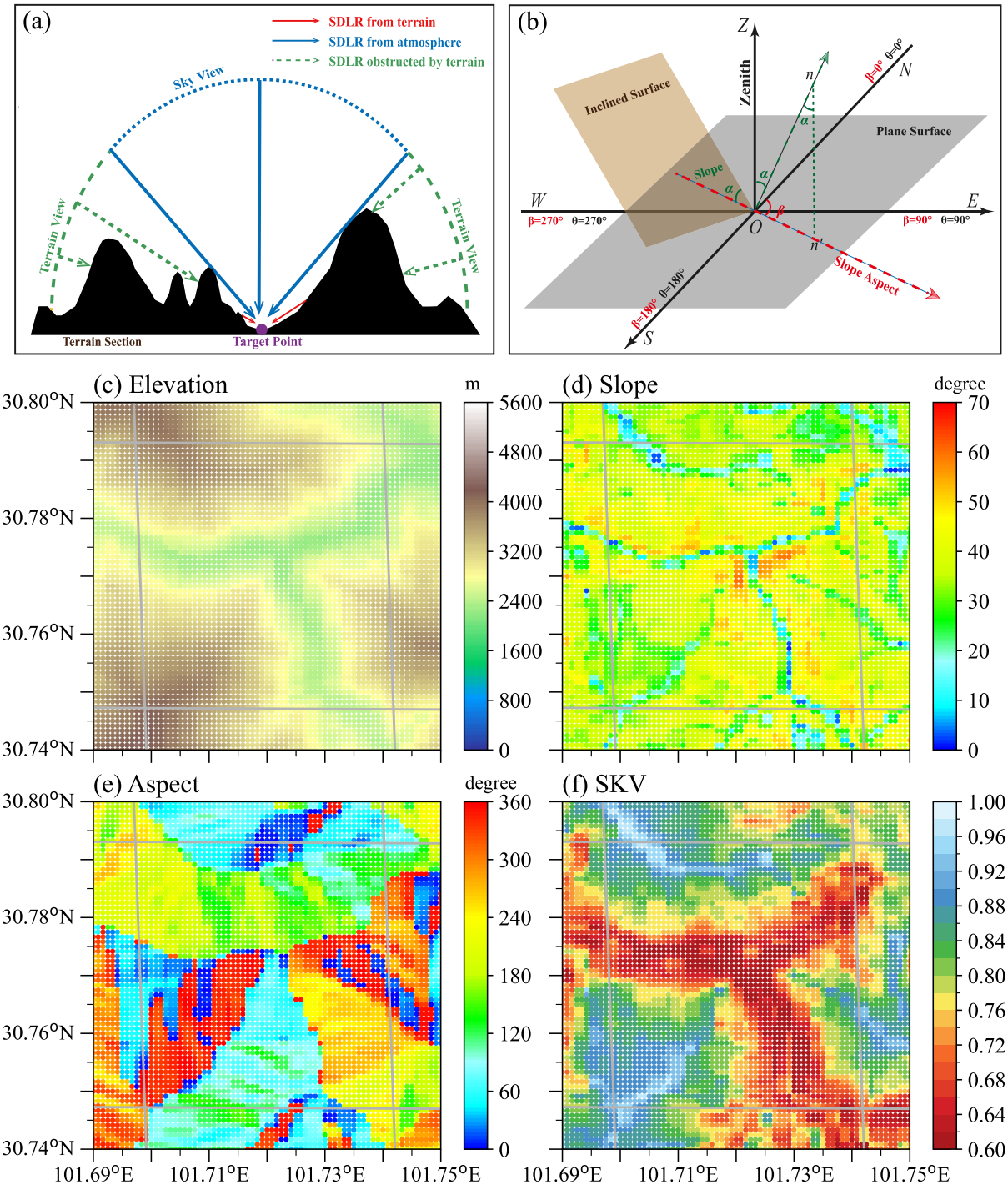


**Figure 2.** (a) Illustrations of components of SDLR over the rugged area. (b) Illustrations of geometric angles for an inclined surface. Distributions of (c) terrain elevation, (d) slope, (e) aspect and (f) the SKV from the DEM data for the rugged region on east side of the Tibet Plateau. The gray lines indicate the borders of FY-4A/AGRI pixels.

where $L_t^{\downarrow}$ is the total SDLR over rugged terrains at AGRI pixel scale, and $N$ is the number of sub-pixel points within an AGRI pixel.

Therefore, according to Equation 1, the explicit calculation expression for SDLR at pixel scale in rugged areas is

$$L_t^{\downarrow} = \frac{1}{N}\sum_{i=1}^{N}\left[L_{p,i}^{\downarrow}\cdot SKV_i\cdot \sec S_i + L_{sur,i}\cdot(1-SKV_i)\cdot \sec S_i\right] \Big/ \frac{1}{N}\sum_{i=1}^{N}\sec S_i. \tag{4}$$

For DA purposes, it is necessary to establish parameterization for Equation 4. The homogenous assumption is adopted for the thermal conditions within the pixel scale, which hypothesizes that the LST $t_{s,i}$, LSE $\varepsilon_{s,i}$ and the near-surface atmospheric temperature $t_{a,i}$ at the $i^{th}$ sub-pixel point within an AGRI pixel of 4-km horizontal resolution are uniform ($t_{s,i} \doteq t_s, \varepsilon_{s,i} \doteq \varepsilon_s, t_{a,i} \doteq t_a$). In other words, SLDR fluxes differences calculated between the pixel and its sub-pixels are assumed to be negligible ($L_{p,i}^{\downarrow} \doteq L_p^{\downarrow}$, $L_{sur,i} \doteq L_p^{\uparrow}$), where $L_p^{\downarrow}$ is the downwelling atmospheric radiance and $L_p^{\uparrow}$ is the upwelling surface long-wave radiance, respectively, at pixel scale.

Therefore, Equation 4 is rewritten as

$$L_t^{\downarrow} = L_p^{\downarrow}\cdot P_1 + L_p^{\uparrow}\cdot P_2 \tag{5}$$

where the two terrain correction parameters $P_1 = \sum_{i=1}^{N} SKV_i\cdot\sec S_i \Big/ \sum_{i=1}^{N}\sec S_i$ and $P_2 = \sum_{i=1}^{N}(1-SKV_i)\cdot \sec S_i \Big/ \sum_{i=1}^{N}\sec S_i$ are not dependent on real-time atmospheric and surface conditions. The time-consuming part of calculation of the $P_1$ and $P_2$ from the DEM data are established only once in advance before application.

The STLRE scheme is basically derived from Gu et al. (2024), which was implemented in atmospheric numerical models to describe the sub-pixel terrain effect on long-wave radiation transfer over mountainous regions. Similar but not identical to the previous study of Gu et al. (2024), the STLRE scheme is applied in the fast radiative transfer model to describe the sub-pixel terrain long-wave effect at AGRI pixels, not at atmospheric model grids. It means that DEM data of 90 m resolution are collocated within the 4 km AGRI pixel to derive the terrain-related parameters. Additionally, the radiation-related variable here represents the radiance at a specific satellite infrared wavelength band rather than the broadband radiance. Theoretically, the STLRE is suitable for either the broadband radiance or a specific wavelength band. Since the radiative terms and parameters for a specific wavelength band, such as the atmospheric downwelling longwave radiance, the surface emissivity and the atmospheric transmittance, can be simulated by the CRTM, the spectral dependency of thermal energy is well described. Therefore, the terrain correction parameters of the STLRE scheme which describes the geometric effects can be reasonably applied to determine the weight of radiance adjustment at a specific wavelength.

The STLRE scheme is then applied to the CRTM. The radiance at top of atmosphere that is contributed by the surface upward radiative term under the plane-parallel condition, that is, $L_{surface,p}$, includes the surface emissive radiance and surface reflection of downwelling radiance,

$$L_{surface,p} = \varepsilon_s\cdot \mathrm{T}(p_s,\cos\theta)\cdot B(t_s) + (1-\varepsilon_s)\cdot \mathrm{T}(p_s,\cos\theta)\cdot\int_0^{p_s} B(t_p)\frac{\partial \mathrm{T}(p,\cos\theta)}{\partial(\ln p)}d(\ln p) \tag{6}$$

where $\varepsilon_s$ is the surface emissivity, $\mathrm{T}(p_s,\cos\theta)$ is the transmittance from the surface to the TOA in the satellite observation direction, $B(t_s)$ is the Planck function of LST, $B(t_p)$ is the Planck function of temperature at pressure $p$ , and $\mathrm{T}(p,\cos\theta)$ is the transmittance from pressure $p$ to the TOA.

According to Equation 5, the $L_p^{\downarrow}$ radiance is $\int_0^{p_s} B(t_p)\frac{\partial \mathrm{T}(p,\cos\theta)}{\partial(\ln p)}d(\ln p)$, while the $L_p^{\uparrow}$ radiance is $\varepsilon_s\cdot B(t_s)$. Therefore, the surface radiative term over the rugged areas, that is, $L_{surface,t}$, is modified as,

$$\begin{aligned} L_{surface,t} &= \varepsilon_s\cdot \mathrm{T}(p_s,\cos\theta)\cdot B(t_s) + \\ &(1-\varepsilon_s)\cdot \mathrm{T}(p_s,\cos\theta)\cdot\left[\int_0^{p_s} B(t_p)\frac{\partial \mathrm{T}(p,\cos\theta)}{\partial(\ln p)}d(\ln p)\cdot P_1 + \varepsilon_s\cdot B(t_s)\cdot P_2\right]. \end{aligned} \tag{7}$$

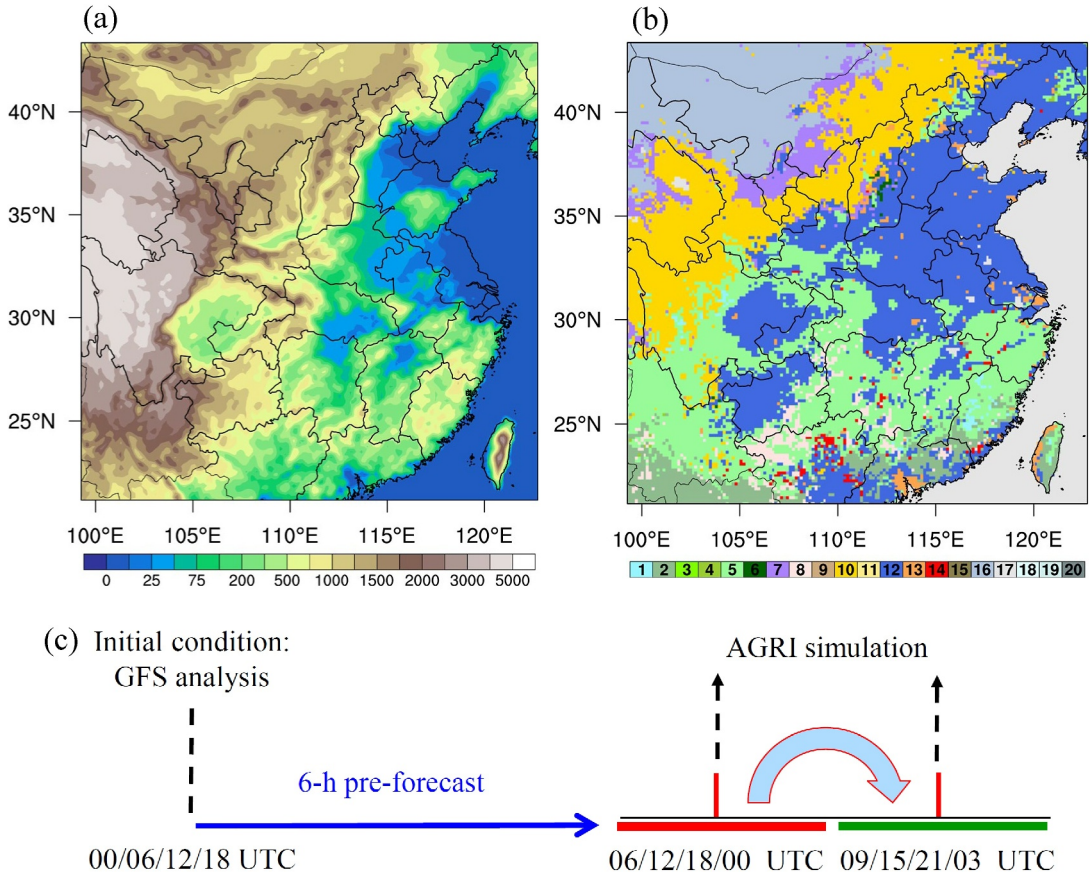


**Figure 3.** (a) The terrain height (color shaded; unit: m) of the WRF model domain. (b) Spatial distributions of IGBP land cover types: (1) Evergreen Needleleaf Forest, (2) Evergreen Broadleaf Forest, (3) Deciduous Needleleaf Forest, (4) Deciduous Broadleaf Forest, (5) Mixed Forests, (6) Closed Shrublands, (7) Open Shrublands, (8) Woody Savannas, (9) Savannas (10) Grasslands (11) Permanent Wetlands (12) Croplands (13) Urban and Built-Up (14) Cropland/Natural Vegetation Mosaic (15) Snow and Ice (16) Barren or Sparsely Vegetated (17) Water (18) Wooded Tundra (19) Mixed Tundra, and (20) Barren Tundra. (c) Schematic illustration of the data assimilation cycling designed for the AGRI TB simulation.

In the rugged areas, according to Equation 5, if the sub-pixel terrain slopes are uniform within the pixel, $P_1 \doteq \frac{1}{N}\sum_{i=1}^{N} SKV_i$ and $P_2 \doteq 1 - P_1$, where $\frac{1}{N}\sum_{i=1}^{N} SKV_i$ is the pixel-scale SKV aggregated from sub-pixels within a pixel. Compared with the traditional plane-parallel scheme, the simulation differences of radiance is

$$\delta L_{surface} = (1-\varepsilon_s)\cdot \mathrm{T}(p_s, \cos\theta)\cdot\left[\varepsilon_s \cdot B(t_s)\cdot P_2 - \int_0^{p_s} B(t_p)\frac{\partial \mathrm{T}(p,\cos\theta)}{\partial(\ln p)} d(\ln p)\cdot(1-P_1)\right]. \quad (8)$$

As a result, the sub-pixel terrain impact on TB simulation is attributed to the reflection of SDLR.

### 2.3. Experimental Design

The ARW-WRF version 3.9.1 is employed as the forecasting model in this study. The forecasts are produced at a 15-km resolution in a domain of 163 × 163 horizontal grid points, covering central and eastern China (Figure 3a). Complex terrains including the eastern slope of the Tibetan Plateau, the Qinling Mountains and the hilly region along the southeast coast are located in the domain. The model has 48 vertical levels extending from the surface to about 10 hPa. Physical parameterization schemes (Skamarock et al., 2008) include the Rapid Radiative Transfer Model longwave radiation, the Dudhia shortwave radiation, the WRF single-moment 6-class (WSM6) microphysics, the Yonsei University planetary boundary layer, the Monin–Obukhov surface layer, the Noah land surface and the Kain-Fritsch cumulus schemes. The land type uses the International Geosphere-Biosphere Program (IGBP) classification. In central and eastern China, the land surface is mostly covered by different kinds of

forests in the southern part, by cropland in the middle part, and by grassland, shrubland and barren in the northern part (Figure 3b).

Model forecasts are launched every 6 hr with the atmospheric initial and boundary conditions provided by the NCEP GFS global analyses and forecasts data which have the horizontal resolution of 0.25° × 0.25°. After a 6-hr pre-forecast, the AGRI clear-sky TBs are simulated by the CRTM at a 3-hr interval. Specifically, the forecasts valid at 0600, 1200, 1800, 0000 and 0300 UTC, are initialized from 0000, 0600, 1200 and 1800 UTC on each day during June 2022 to May 2023, respectively (Figure 3c). Therefore, eight samples at 3-hr intervals are generated every day, which mimic a realistic O-B performance in regional DA. AGRI TBs are simulated and compared with the observations. Two experiments are conducted to explore the benefits of modified observation operators with the consideration of STLRE. The control experiment (ExpCTL) applies the default CRTM without the STLRE while the other experiment (ExpTOPO) employs the modified CRTM considering the STLRE to simulate the AGRI TBs over land. For the calculations of O-B in ExpCTL and ExpTOPO, the observed TBs provided by AGRI are the same, while the simulated TBs are calculated by default CRTM and modified CRTM, respectively.

## 3. Results

To avoid the systematic TB O-B biases related to potential LST, LSE and other uncertainties in the radiative transfer simulations, we analyze the terrain residual biases $\overline{O-B-\mu_p(\theta,\varphi)}$ with the averaged biases of flat areas $\mu_p(\theta,\varphi)$ removed. The $\mu_p(\theta,\varphi)$ are sampled by the data of pixel-scale aggregated SKV larger than 0.99 within 1° × 1° latitudinal and longitudinal boxes separately for daytime and nighttime in different months. Excluding the systematic biases, the residual biases $\overline{O-B-\mu_p(\theta,\varphi)}$ can better characterize the biases caused by insufficient considerations of terrain impact in RTM.

Results of AGRI TB simulations by the default CRTM show orography dependent biases in rugged terrain areas. Figure 4 displays the distributions of aggregated SKV at AGRI pixel-scale and the clear-sky TB O-B biases of channel 11 (8.6 μm), channel 12 (10.8 μm) and channel 13 (12.0 μm) from ExpCTL averaged within 1° × 1° grid boxes in the simulation domain using the 1-year data sample. The regional mean helps to show the geographic distribution of TB biases. It shows obvious positive biases in the eastern slope of the Tibet Plateau (around 102°E, 30°N) and the Qinling Mountains (around 109°E, 32°N), and slight positive biases in the Zhejiang-Fujian hilly regions (around 119°E, 27°N) and the Guangxi-Hunan hilly regions (around 107°E, 25°N). It indicates the surface-sensitive TBs are underestimated by the default CRTM which ignores the STLRE. The limitation of the traditional observation operator restricts the effective AGRI DA over rugged areas.

Two typical regions are selected to compare the AGRI TB simulations between the default and the modified CRTM. Figures 5a, 5b, 5f, and 5h show the distributions of AGRI clear-sky O-B biases for channel 12 in region 1 (eastern slope of the Tibetan Plateau) and region 2 (Qinling Mountains) at 1800 UTC 29 January 2023, simulated by ExpCTL and ExpTOPO, respectively. This scene is selected for a wide expanse of clear sky. In region 1, the terrain residual biases produced by the ExpCTL with the intensity up to 0.6 K is located in the areas east to 101°E (Figure 5a), while the biases produced by the ExpTOPO are much closer to zero within the range of about −0.2 ∼ 0.3 K (Figure 5b). In region 2, the terrain residual biases produced by the ExpCTL are about 0.4 ∼ 0.7 K and situated along the west-east oriented mountains around 32°N (Figure 5f), while the biases produced by the ExpTOPO can be reduced to about −0.2 ∼ 0.2 K (Figure 5g). The simulated TB differences between ExpTOPO and ExpCTL (ExpTOPO minus ExpCTL) show negative patterns (Figures 5c and 5h), suggesting the ExpTOPO reasonably compensates the positive TB O-B biases that are revealed in ExpCTL (Figures 5a and 5f). Theoretically, the SDLR over rugged areas are weighted by both of the atmospheric downwelling radiance and the radiance emitted by surrounding terrain. Without considering the STLRE in ExpCTL, the simulated downwelling radiance is only contributed by the atmospheric downwelling radiance, which are usually smaller than the terrain emissive radiance because of positive land-air temperature difference. It causes underestimated downwelling radiance as well as the surface reflection of downwelling radiance. It finally results in underestimated TB simulation and positive O-B bias. Considering the STLRE can clearly reduce the positive biases in the rugged areas indicated by small SKVs (Figures 5d and 5i). These rugged areas generally correspond to the land type of mixed forests or grassland (Figures 5e and 5j).

In addition to single time cases, Figures 6a–6c show the long-term statistical characteristics of residual O-B biases produced by ExpCTL and ExpTOPO experiments with respect to the SKV. The four mountainous regions shown

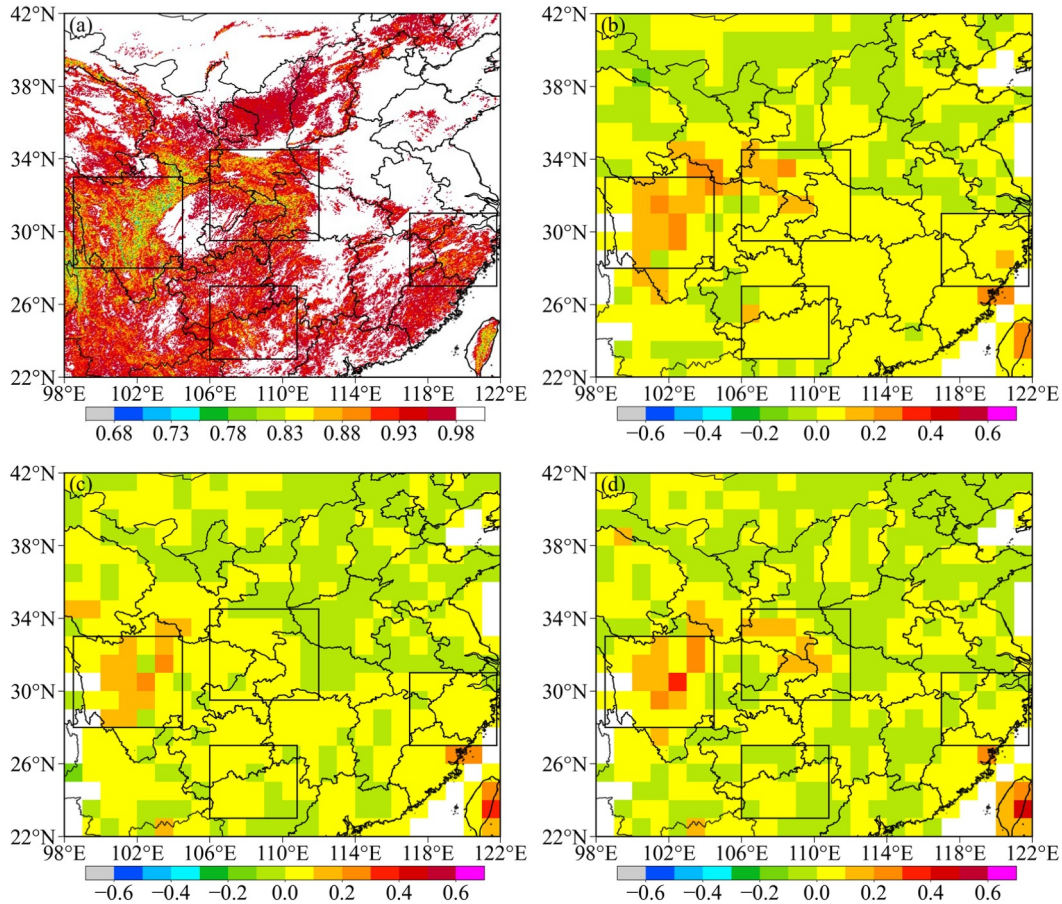


**Figure 4.** (a) Distributions of the SKV aggregated at the FY-4A/AGRI pixel scale. Spatial distributions of O-B-$\mu_p$ biases (unit: K) of ExpCTL for the channels (b) 11, (c) 12 and (d) 13 within 1° × 1° boxes averaged by the clear-sky samples from June 2022 to May 2023. The systematic biases $\mu_p$ at plane surface conditions are subtracted in (b), (c), (d).

in Figure 4a are focused on. As the SKV decreases, the terrain is more complex and the terrain impact on SDLR simulation becomes more obvious. The O-B biases produced by the ExpCTL show increasing trends at all of the three wavelengths. The maximum of O-B biases for the three channels are larger than or close to 0.4 K. It reveals that the default CRTM significantly underestimates the TB values as the terrain complexity increases. In comparison, the O-B biases produced by the ExpTOPO remarkably decrease to close to zero, which shows marginal variation as the SKV varies. Compared to the ExpCTL experiment, the biases produced by the ExpTOPO experiment averaged over the regions with the SKV less than 0.8 can be reduced by 64.2%, 72.7% and 67.6% for the channels 11, 12 and 13, respectively. By considering the STLRE, the total SDLR produced by the ExpTOPO experiment is increased in the rugged areas. The reflection of SDLR in the RTM (Equation 7) leads to larger TB simulated values. Therefore, the ExpTOPO experiment produces lower O-B biases than the ExpCTL experiment. The root mean square errors (RMSEs) calculated by the O-B of AGRI channel 11–13 are shown in Figures 6d–6f. As the SKV decreases, the RMSEs become smaller in the ExpTOPO experiment than in the ExpCTL experiment, implying that the modified observation operator effectively improves the TB simulation accuracy in the rugged areas.

Because the infrared DA in regional models requires geostationary satellite data with high temporal frequency, we also examine the TB simulation performance at different times of the day for the ExpCTL and ExpTOPO experiments. Figure 7 shows the diurnal variations of O-B residual biases and the RMSEs for the AGRI channels 11–13. The clear-sky data pixels with the SKV less than 0.85 are employed to represent the rugged areas. For channel 11, about 0.2 K positive biases are found in the ExpCTL experiment throughout the day. With the STLRE, the ExpTOPO reduces the biases to nearly zero (Figure 7a). For the channels 12 and 13, as compared to the ExpCTL experiment, the ExpTOPO experiment also reduces the biases with the magnitude of 0.2 ∼ 0.3 K

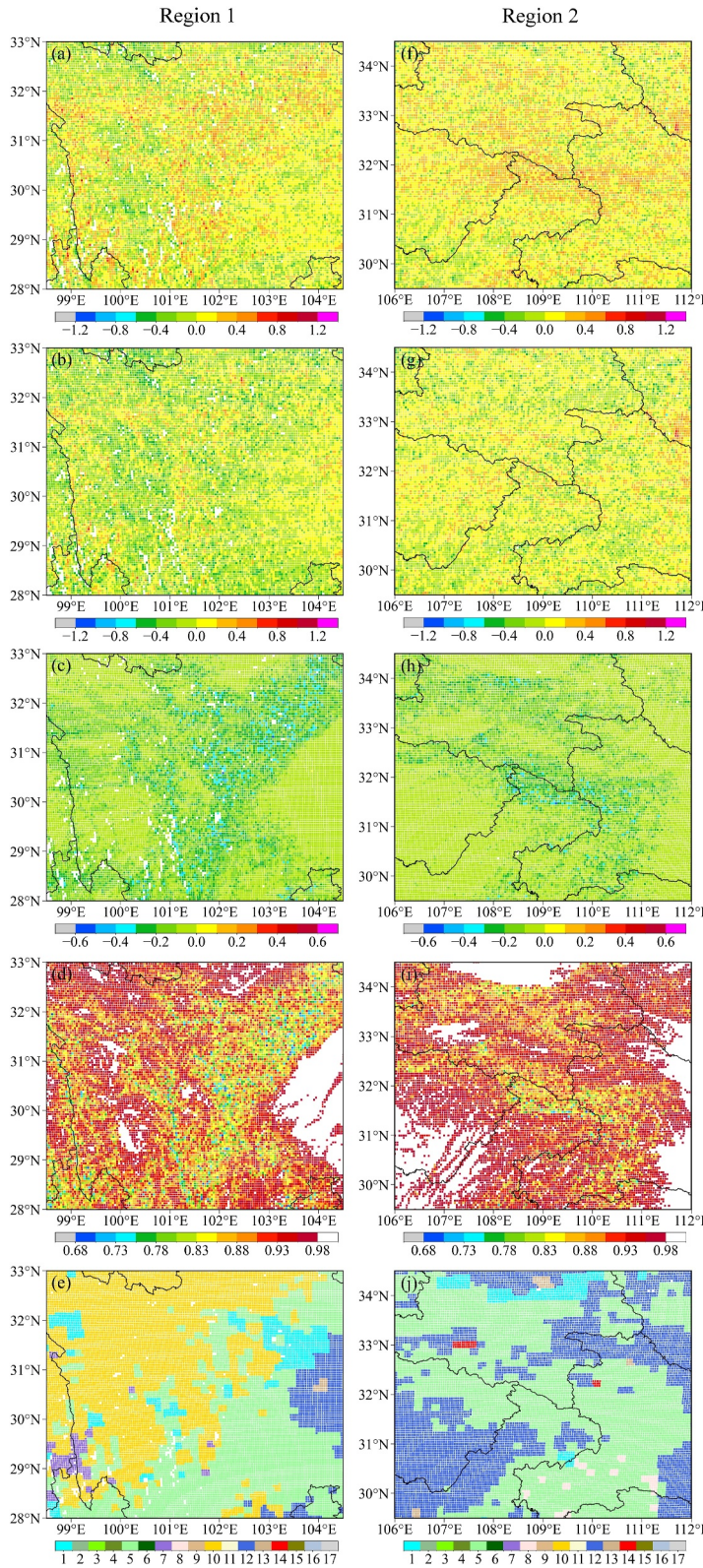


**Figure 5.** Distributions of AGRI clear-sky TB O-B-$\mu_p$ (unit: K) for channel 12 in (a), (b) region 1 (eastern slope of the Tibetan Plateau) and (f), (g) region 2 (Qinling Mountains) at 1800 UTC 29 January 2023, for (a), (f) ExpCTL and (b), (g) ExpTOPO experiments (c), (h) Distributions of clear-sky TB differences calculated by ExpTOPO minus ExpCTL for (c) region 1 and (h) region 2 (d), (i) Distributions of the SKV for (d) region 1 and (i) region 2 (e), (j) Distributions of the land types for (e) region 1 and (j) region 2. The meaning of land type indices are the same as that in Figure 3.

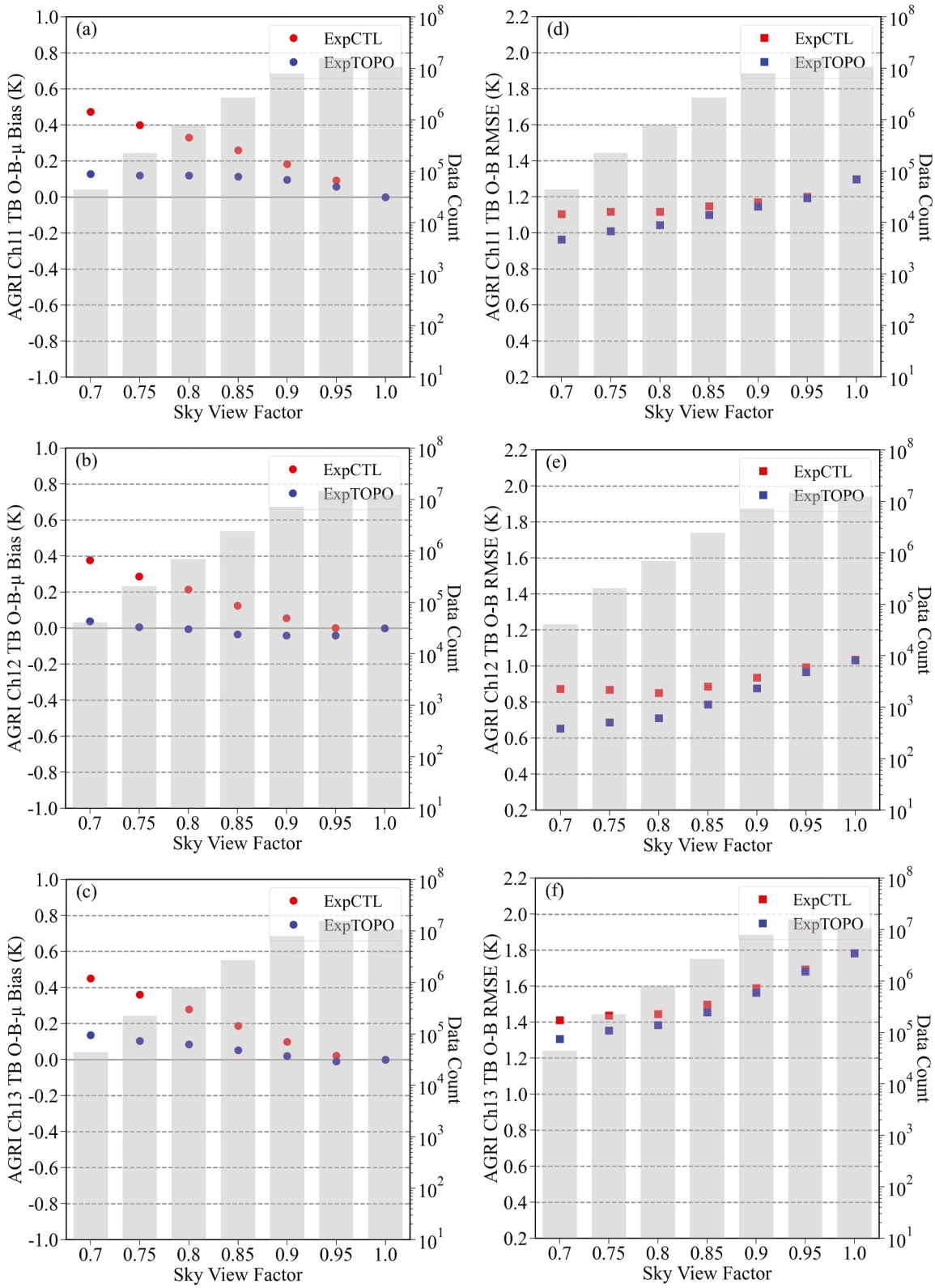


**Figure 6.** Averaged clear-sky (a)–(c) O-B-$\mu_p$ biases and (d)–(f) RMSEs calculated by the O-B for AGRI channels (a), (d) 11 (b), (e) 12 and (c), (f) 13 with respect to the SKV for the ExpCTL and ExpTOPO experiments from June 2022 to May 2023. The gray bars indicate the total data count at each bin of SKV.

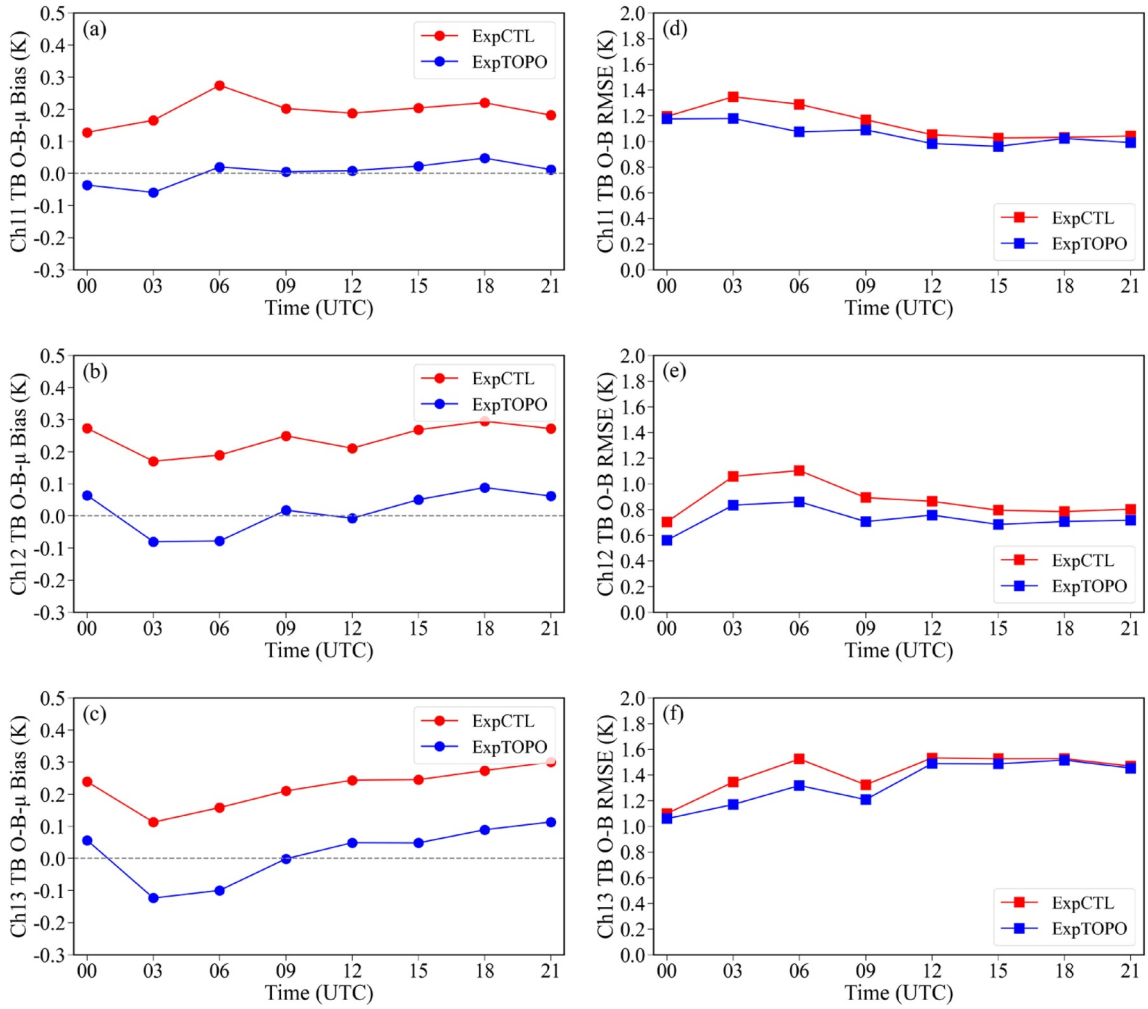


**Figure 7.** Diurnal variations of averaged clear-sky (a)–(c) O-B-$\mu_p$ biases and (d)–(f) RMSEs calculated by the O-B for AGRI channels (a), (d) 11 (b), (e) 12 and (c), (f) 13 for the ExpCTL and ExpTOPO experiments from June 2022 to May 2023. The data pixels are obtained under conditions that the SKV less than 0.85.

(Figures 7b and 7c). The diurnal fluctuations of O-B biases for the two channels are less than 0.2 K. The maximum reductions of the simulated TB RMSEs are up to 0.2 K in the ExpTOPO compared to the ExpCTL (Figures 7d–7f) for all the three channels. We can see stable improvements of TB simulation at different times of the day over rugged areas due to considering the STLRE in CRTM.

We further investigate the simulated differences between the ExpTOPO and ExpCTL experiments over the rugged areas in different months and under different land cover types. Figure 8 displays the mean TB simulated differences as well as the mean LSE at the clear-sky pixels with the SKV less than 0.85. The TB simulation differences directly reflect the impact of STLRE. The TB simulation differences at three wavelengths are maximum in winter (about 0.2 ∼ 0.3 K), followed by spring and autumn, and minimum in summer (about 0.1 ∼ 0.2 K). Moreover, the monthly variations of TB simulation differences are larger in channel 11 than in channels 12 and 13 (Figure 8a). Under different land surfaces classified by the IGBP land cover types, the TB simulation differences are the largest under Barren or Sparsely Vegetated (about 0.3 ∼ 0.4 K), followed by Open Shrublands, Grasslands, Evergreen Needleaf Forest and Mixed Forests, while the smallest under Croplands, Woody Savannas and Evergreen Broadleaf Forest (about 0.1 ∼ 0.2 K) (Figure 8b).

According to Equation 8, the TB simulation differences between the ExpTOPO and ExpCTL experiments theoretically come from the differences between the terrain emissive radiance and atmospheric downwelling radiance, which is proportional to the land-air temperature differences. As shown in Figures 9a–9c and 9e, the TB

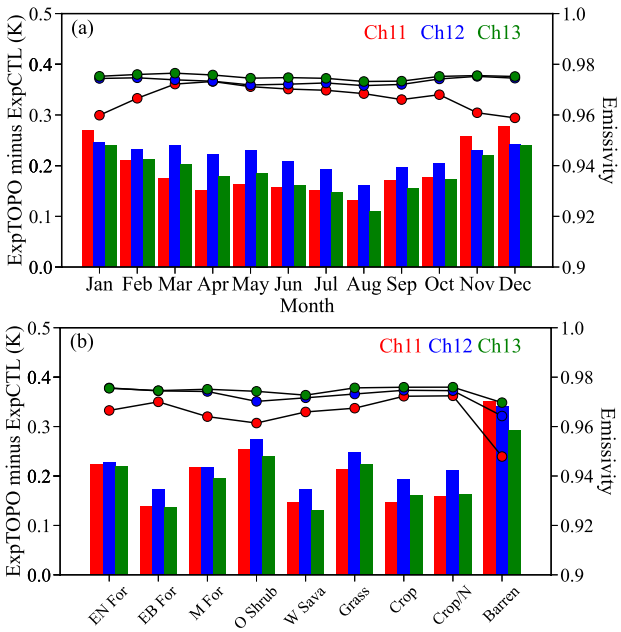


**Figure 8.** Averaged clear-sky TB simulated differences between ExpTOPO and ExpCTL, as well as averaged emissivity (solid lines with dots) for channels 11–13, as variations to (a) different months and (b) different land types, under conditions that the SKV less than 0.85.

simulation differences with respect to the SKV under four levels of land-air temperature differences, the simulation differences for all the three channels increase as the land-air temperature differences gradually increase. Since the mean land-air temperature differences are higher in winter than in summer (not shown), the TB simulation correction in the ExpTOPO experiment is the greatest in winter (Figure 8a).

In addition, according to Equation 8, the TB simulation differences are inversely proportional to the LSE. Figures 9b–9d and f show the TB simulation differences with respect to the SKV under four levels of LSE. As the LSE gradually decreases, the simulation differences increase for all the three channels (Figures 9b, 9d and 9f). The larger corrections of TB simulations under Barren or Sparsely Vegetated type are attributed to the smaller LSE (Figure 8b). Also, the LSE is smaller in winter than in other seasons (Figures 1c and 1d) over the rugged regions with the SKV less than 0.85, and the LSE at the wavelength of channel 11 is smaller than the other two wavelengths. This explains why the variations of TB simulation differences between two schemes are larger in channel 11 than in channels 12 and 13 (Figure 8a).

## 4. Conclusion and Discussion

In current RTM, the radiative transfer near surface is based on the plane-parallel scheme, which ignores the impact of terrain undulation on the surface downwelling long-wave radiance (SDLR). The sub-pixel terrain long-wave radiative effect (STLRE) are important to satellite surface-sensitive infrared TB simulation over rugged areas. However, the absence of STLRE limits the numerical models to effectively assimilate satellite data over land. This study incorporates a STLRE scheme, which considers both the obstruction of atmospheric downwelling radiance and the surrounding terrain emissive radiance into the CRTM for the FY-4A/AGRI TB simulations. The TB simulation performance is focused on the rugged areas.

The DEM data with the horizontal resolution of 3″ are applied to describe the sub-pixel terrain parameters such as the elevation, slope, aspect and sky view factor (SKV). Compared to flat areas, the total SDLR at sub-pixel scale over rugged areas is composed of the SDLR from atmosphere and the long-wave radiance emitted from surrounding terrains, weighted by the SKV. Based on the homogenous assumption for the thermal conditions within the pixels, a STLRE scheme is established at pixel scale. The static terrain correction factors for every AGRI pixel point are calculated once using the sub-pixel terrain parameters. In the CRTM, the reflection of SDLR at AGRI pixel scale is then modified according to the terrain correction factors.

Experiments ExpCTL (ExpTOPO) are conducted to evaluate the AGRI clear-sky TB simulations of channels 11–13 over rugged areas using the default (modified) CRTM, during 2022∼2023. To mimic the regional data assimilation, the WRF forecasting fields at 3-hr intervals are used as atmospheric input to CRTM embedded in the GSI DA system. The FY-4A/AGRI land surface temperature product and the UW_HSRemis land surface emissivity are used as the surface parameters input.

Statistical results of AGRI O-B show that without considering the STLRE tends to underestimate the TB over the rugged regions. In the traditional scheme, ignoring the effect of downwelling radiances emitted by the surrounding terrain causes underestimated downwelling radiances during the radiative transfer simulation, which results in underestimated TB simulation and positive O-B biases. The simulation biases are proportional to the terrain complexity and increase with the SKV decreasing in the ExpCTL experiment. Considering the STLRE in CRTM in the ExpTOPO experiment can clearly reduce the orography dependent simulation biases. The mean reduction of O-B biases over rugged areas are 64.2%, 72.7% and 67.6% for the three wavelengths, respectively. These corrections are found stable at different times of a day, which is important for regional data assimilation purposes. Besides, the corrections induced by the consideration of STLRE are found more obvious in winter than

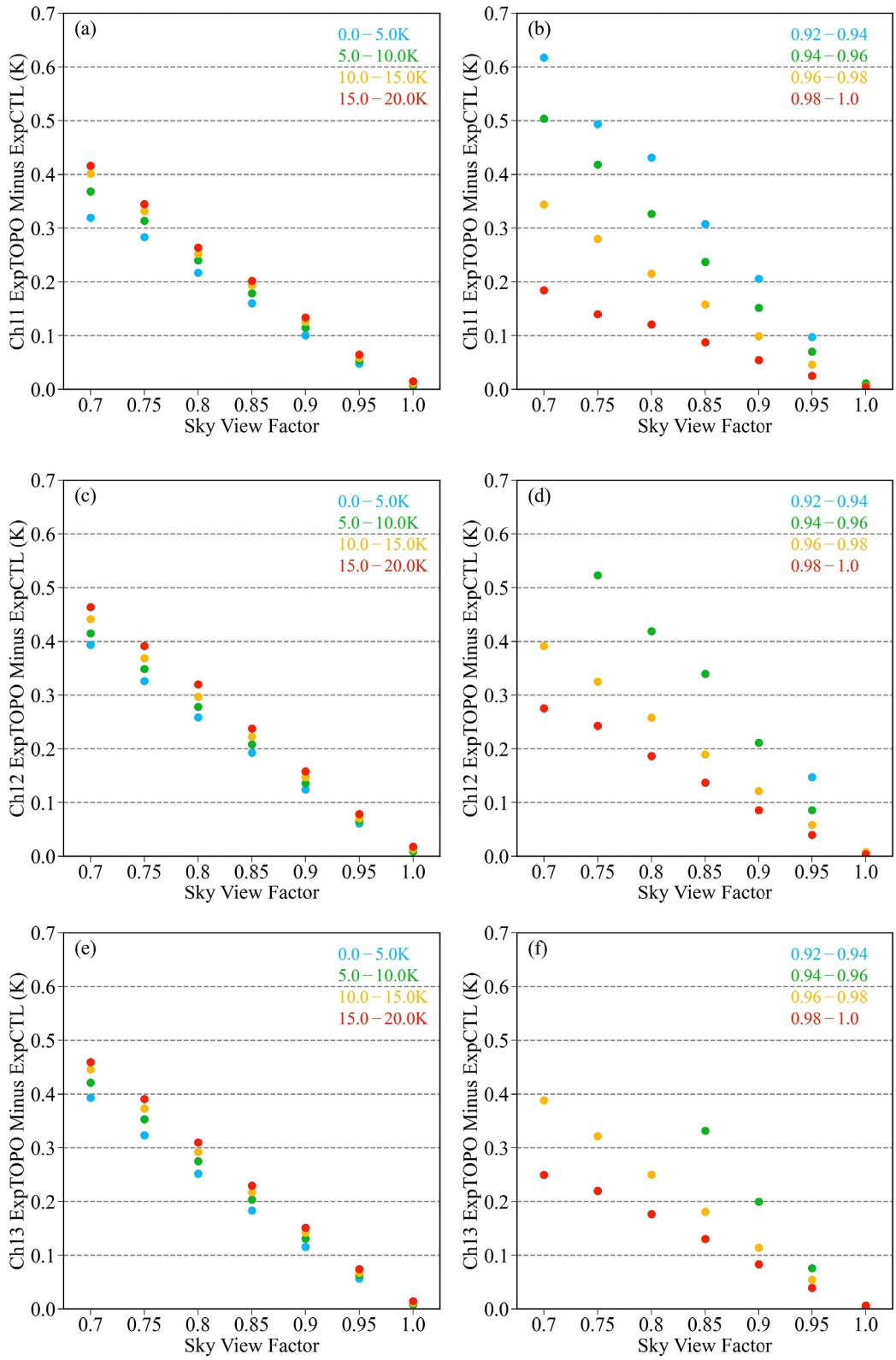


**Figure 9.** Averaged TB simulated differences between the ExpTOPO and ExpCTL experiments for the AGRI channels (a), (b) 11 (c), (d) 12 and (e), (f) 13 with respect to the SKV under the conditions of different land-air temperature differences (a), (c), (e), and different LSEs (b), (d), (f).

in summer, and under the barren condition than under other land cover types. This can be mainly attributed to the land-air temperature difference and the LSE.

This study serves as a pilot study to improve the RTM ability for infrared TB simulation of geostationary satellites over complex terrains. Although the simulation results are promising, the following deficiencies due to objective restrictions should be admitted. First, the isotropic assumption of the adjacent terrain emission ignores the differences of the thermal property between the target point and its surrounding topography. Second, the homogenous assumption neglects the differences of thermal features within 4-km AGRI pixels. Third, because of the high-orbit of FY-4A geostationary satellite, the situations of target sub-pixel obstructed by the surrounding sub-pixels are not considered. Future plans are further updating the scheme considering the aspects mentioned above.

Note that the current modified CRTM with STLRE scheme is designed for AGRI, which relies on the pre-established terrain correction factors for its specific pixels. Implementing the scheme within CRTM, the only thing required is to re-weight the emissive and reflective radiative terms using the two terrain correction factors. In practical assimilation, the STLRE scheme can be applied universally to all scenarios because the simulated downwelling radiance under different surface conditions can be easily adjusted by the two terrain correction parameters. In theory, the parameterization could be efficiently applied to the newest version of CRTM or any other RTM by the same way. Further applications for other geostationary satellite instruments require the similar construction of terrain correction factors that are suitable for their pixel scales. Furthermore, for polar-orbiting satellites, the major challenges of applying the STLRE scheme are the none-static locations of field of views and the relative coarser resolution of each footprint. Besides, the TB simulation improvements are encouraging for future DA of satellite surface-sensitive channels over complex terrain. The DA impacts on severe convective forecasts will be assessed in follow-on studies.

## Data Availability Statement

The AGRI brightness temperature observation, LST retrievals and cloud mask products were collected from the National Satellite Meteorological Center of China (http://satellite.nsmc.org.cn/). The DEM data is obtained from the SRTM Digital Elevation Database Version 4.1 with a horizontal resolution of 3″ (Jarvis et al., 2008).

**Acknowledgments**
This research work was supported by the National Key R&D Program of China (2022YFC3080500), the National Natural Science Foundation of China (42322507, 42275167, 42375157), the Jiangsu Provincial Key Technology R&D Program (BE2022851), the Natural Science Foundation of Jiangsu Province (BK20211396), and the Beijige Research Fund of NJIAS (BJG202403). We would like to express our gratitude to the High Performance Computing Center of Nanjing University, and the National Key Scientific and Technological Infrastructure project, "Earth System Numerical Simulation Facility" (EarthLab), for providing the computational resources. We also thank the editor and three anonymous reviewers for their valuable and constructive suggestions that significantly improved the science presentation of this manuscript.

## References

Adams, E., Slaughter, A., McKittrick, L., & Miller, D. (2011). Local terrain-topography and thermal-properties influence on energy and mass balance of a snow cover. *Annals of Glaciology*, *52*(58), 169–175. https://doi.org/10.3189/172756411797252257

Bessho, K., Date, K., Hayashi, M., Ikeda, A., Imai, T., Inoue, H., et al. (2016). An introduction to Himawari-8/9 - Japan's new-generation geostationary meteorological satellites. *Journal of the Meteorological Society of Japan*, *94*(2), 151–183. https://doi.org/10.2151/jmsj.2016-009

Borbas, E. E., & Ruston, B. C. (2010). The RTTOV UWiremis IR land surface emissivity module. *Version 1, NWP SAF Mission Rep. NWPSAF-MO-VS-042*, 24. https://nwpsaf.eu/vs_reports/nwpsaf-mo-vs-042.pdf

Dong, L., Tang, S., Wang, F., Cosh, M. H., Li, X., & Min, M. (2023). Inversion and validation of FY-4A official land surface temperature product. *Remote Sensing*, *15*(9), 2437. https://doi.org/10.3390/rs15092437

Dozier, J., & Frew, J. (1990). Rapid calculation of terrain parameters for radiation modeling from digital elevation data. *IEEE Transactions on Geoscience and Remote Sensing*, *28*(5), 963–969. https://doi.org/10.1109/36.58986

Duguay, C. R. (1995). An approach to the estimation of surface net radiation in mountain areas using remote sensing and digital terrain data. *Theoretical and Applied Climatology*, *52*(1), 55–68. https://doi.org/10.1007/BF00865507

Dutta, S. K., Garand, L., & Heilliette, S. (2016). Assimilation of infrared radiance observations with sensitivity to land surfaces in the Canadian ensemble–variational system. *Journal of Applied Meteorology and Climatology*, *55*(3), 561–578. https://doi.org/10.1175/jamc-d-15-0208.1

English, S. J. (2008). The importance of accurate skin temperature in assimilating radiances from satellite sounding instruments. *IEEE Transactions on Geoscience and Remote Sensing*, *46*(2), 403–408. https://doi.org/10.1109/tgrs.2007.902413

Eyre, J. R., Bell, W., Cotton, J., English, S. J., Forsythe, M., Healy, S. B., & Pavelin, E. G. (2022). Assimilation of satellite data in numerical weather prediction. Part II: Recent years. *Quarterly Journal of the Royal Meteorological Society*, *148*(743), 521–556. https://doi.org/10.1002/qj.4228

Feldman, D. R., Worden, M., Falco, N., Dennedy-Frank, P. J., Chen, J., Dafflon, B., & Wainwright, H. (2022). Three-dimensional surface downwelling longwave radiation clear-sky effects in the upper Colorado river basin. *Geophysical Research Letters*, *49*(4). https://doi.org/10.1029/2021GL094605

Geer, A. J., Migliorini, S., & Matricardi, M. (2019). All-sky assimilation of infrared radiances sensitive to mid-and upper-tropospheric moisture and cloud. *Atmospheric Measurement Techniques*, *12*(9), 4903–4929. https://doi.org/10.5194/amt-12-4903-2019

Gu, C., Huang, A., Li, X., Yang, B., & Wu, Y. (2024). Construction of a clear-sky three dimensional sub-grid terrain long-wave radiative effect parameterization scheme under isotropic assumption. *Journal of Geophysical Research: Atmospheres*, *129*(4). https://doi.org/10.1029/2023JD039383

Guedj, S., Karbou, F., & Rabier, F. (2011). Land surface temperature estimation to improve the assimilation of SEVIRI radiances over land. *Journal of Geophysical Research*, *116*(D14), D14107. https://doi.org/10.1029/2011JD015776

Han, Y., Weng, F., Liu, Q., & van Delst, P. (2007). A fast radiative transfer model for SSMIS upper atmosphere sounding channels. *Journal of Geophysical Research*, *112*(D11), D11121. https://doi.org/10.1029/2006JD008208

He, Z., & Tang, B. (2023). Retrieval of rugged mountainous areas land surface temperature from high-spatial-resolution thermal infrared remote sensing data. *IEEE Transactions on Geoscience and Remote Sensing*, *61*, 4508216. https://doi.org/10.1109/tgrs.2023.3316624

Hilton, F., Armante, R., August, T., Barnet, C., Bouchard, A., Camy-Peyret, C., et al. (2012). Hyperspectral Earth observation from IASI: Five years of accomplishments. *Bulletin America Meteorology Social*, *93*(3), 347–370. https://doi.org/10.1175/BAMS-D-11-00027.1

Honda, T., Miyoshi, T., Lien, G. Y., Nishizawa, S., Yoshida, R., Adachi, S. A., et al. (2018). Assimilating all-sky himawari-8 satellite infrared radiances: A case of typhoon soudelor (2015). *Monthly Weather Review*, *146*(1), 213–229. https://doi.org/10.1175/MWR-D-16-0357.1

Huang, A., Gu, C., Zhang, Y., Li, W., Zhang, L., Wu, Y., et al. (2022). Development of a clear-sky 3D sub-grid terrain solar radiative effect parameterization scheme based on the mountain radiation theory. *Journal of Geophysical Research: Atmospheres*, *127*(13). https://doi.org/10.1029/2022jd036449

Jarvis, A., Reuter, H. I., Nelson, A., & Guevara, E. (2008). The Shuttle radar topography mission (SRTM) 90m digital elevation Database v4.1 [Dataset]. *International Centre for Tropical Agriculture (CIAT)*. Retrieved from https://developers.google.com/earth-engine/datasets/catalog/CGIAR_SRTM90_V4

Jiao, Z.-H., Ren, H., Mu, X., Zhao, J., Wang, T., & Dong, J. (2019). Evaluation of four sky view factor algorithms using digital surface and elevation model data. *Earth and Space Science*, *6*(2), 222–237. https://doi.org/10.1029/2018EA000475

Li, J., & Liu, H. (2009). Improved hurricane track and intensity forecast using single field-of-view advanced IR sounding measurements. *Geophysical Research Letters*, *36*(11), L11813. https://doi.org/10.1029/2009GL038285

Li, X., Zou, X., Zeng, M., Wang, N., & Tang, F. (2021). Exploring the assimilation of ATMS cloud retrieval products and its benefits for CrIS all-sky radiance simulations. *Monthly Weather Review*, *149*, 1873–1901. https://doi.org/10.1175/MWR-D-20-0345.1

Li, X., Zou, X., Zeng, M. J., Zhuge, X., & Liu, W. (2023). Improving AHI radiance assimilation over land with the surface skin temperature constrained by station observations and its impact for quantitative precipitation forecasts. *Monthly Weather Review*, *151*(11), 2925–2947. https://doi.org/10.1175/MWR-D-23-0052.1

Okamoto, K., Sawada, Y., & Kunii, M. (2019). Comparison of assimilating all-sky and clear-sky infrared radiances from Himawari-8 in a mesoscale system. *Quart. J. Roy. Meteor. Soc.*, *145*(719), 745–766. https://doi.org/10.1002/qj.3463

Oliphant, A. J., Spronken-Smith, R. A., Sturman, A. P., & Owens, I. F. (2003). Spatial variability of surface radiation fluxes in mountainous terrain. *Journal of Applied Meteorology*, *42*(1), 113–128. https://doi.org/10.1175/1520-0450(2003)042<0113:svosrf>2.0.co;2

Otkin, J. A., & Potthast, R. (2019). Assimilation of all-sky SEVIRI infrared brightness temperatures in a regional-scale ensemble data assimilation system. *Monthly Weather Review*, *147*(12), 4481–4509. https://doi.org/10.1175/mwr-d-19-0133.1

Pavelin, E. G., & Candy, B. (2014). Assimilation of surface-sensitive infrared radiances over land: Estimation of land surface temperature and emissivity. *Quarterly Journal of the Royal Meteorological Society*, *140*(681), 1198–1208. https://doi.org/10.1002/qj.2218

Proy, C., Tanré, D., & Deschamps, P. Y. (1989). Evaluation of topographic effects in remotely sensed data. *Remote Sensing of Environment*, *30*(1), 21–32. https://doi.org/10.1016/0034-4257(89)90044-8

Qin, Z., & Zou, X. (2019). Impact of AMSU-A data assimilation over high terrains on QPFs downstream of the Tibetan Plateau. *J. Meteor. Soc. Japan*, *97*(6), 1137–1154. https://doi.org/10.2151/jmsj.2019-064

Robledano, A., Picard, G., Arnaud, L., Larue, F., & Ollivier, I. (2022). Modelling surface temperature and radiation budget of snow-covered complex terrain. *The Cryosphere*, *16*(2), 559–579. https://doi.org/10.5194/tc-16-559-2022

Sawada, Y., Okamoto, K., Kunii, M., & Miyoshi, T. (2019). Assimilating every-10-minute Himawari-8 infrared radiances to improve convective predictability. *Journal of Geophysical Research: Atmospheres*, *124*(5), 2546–2561. https://doi.org/10.1029/2018jd029643

Schmit, T., Griffith, P., Gunshor, M., Daniels, J., Goodman, S., & Lebair, W. (2017). A closer look at the ABI on the GOES-R series. *Bulletin America Meteorology Social*, *98*(4), 681–698. https://doi.org/10.1175/BAMS-D-15-00230.1

Sicart, J. E., Pomeroy, J. W., Essery, R. L. H., & Bewley, D. (2006). Incoming longwave radiation to melting snow: Observations, sensitivity and estimation in northern environments. *Hydrological Processes*, *20*(17), 3697–3708. https://doi.org/10.1002/hyp.6383

Skamarock, W. C., & Coauthors (2008). A description of the Advanced Research WRF version 3. *NCAR Tech. Note NCAR/TN-4751STR*, 113. https://doi.org/10.5065/D68S4MVH

Tang, F., Zhuge, X., Zeng, M., Li, X., Dong, P., & Han, Y. (2021). Applications of the advanced radiative transfer modeling system (ARMS) to characterize the performance of fengyun–4A/AGRI. *Remote Sensing*, *13*(16), 3120. https://doi.org/10.3390/rs13163120

Wang, X., Min, M., Wang, F., Guo, J., Li, B., & Tang, S. (2019). Intercomparisons of cloud mask products among fengyun-4a, himawari-8, and modis. *IEEE Transactions on Geoscience and Remote Sensing*, *57*(11), 8827–8839. https://doi.org/10.1109/tgrs.2019.2923247

Weng, F. (2007). Advances in radiative transfer modeling in support of satellite data assimilation. *Journal of the Atmospheric Sciences*, *64*(11), 3799–3807. https://doi.org/10.1175/2007jas2112.1

Xu, D., Liu, Z., Fan, S., Chen, M., & Shen, F. (2021). Assimilating all-sky infrared radiances from himawari-8 using the 3DVar method for the prediction of a severe storm over north China. *Advances in Atmospheric Sciences*, *38*(4), 661–676. https://doi.org/10.1007/s00376-020-0219-z

Xue, Y., Zhu, X., Wu, Z., & Duan, S.-B. (2023). Retrieval of land surface temperature over mountainous areas using fengyun-3D MERSI-II data. *Remote Sensing*, *15*(23), 5465. https://doi.org/10.3390/rs15235465

Yan, G., Jiao, Z. H., Wang, T., & Mu, X. (2020). Modeling surface longwave radiation over high-relief terrain. *Remote Sensing of Environment*, *237*, 111556. https://doi.org/10.1016/j.rse.2019.111556

Yan, G., Wang, T., Jiao, Z., Mu, X., Zhao, J., & Chen, L. (2016). Topographic radiation modeling and spatial scaling of clear-sky land surface longwave radiation over rugged terrain. *Remote Sensing of Environment*, *172*, 15–27. https://doi.org/10.1016/j.rse.2015.10.026

Yang, J., Zhang, Z., Wei, C., Lu, F., & Guo, Q. (2016). Introducing the new generation of Chinese geostationary weather satellites, Fengyun-4. *Bulletin America Meteorology Social*, *98*(8), 1637–1658. https://doi.org/10.1175/BAMS-D-16-0065.1

Yin, R., Han, W., Gao, Z., & Li, J. (2021). Impact of high temporal resolution FY-4A Geostationary Interferometric Infrared Sounder (GIIRS) radiance measurements on Typhoon forecasts: Maria (2018) case with GRAPES global 4D-Var assimilation system. *Geophysical Research Letters*, *48*(15), e2021GL093672. https://doi.org/10.1029/2021GL093672

Zhang, F., Minamide, M., & Clothiaux, E. E. (2016). Potential impacts of assimilating all-sky infrared satellite radiances from GOES-R on convection-permitting analysis and prediction of tropical cyclones. *Geophysical Research Letters*, *43*(6), 2954–2963. https://doi.org/10.1002/2016GL068468

Zhang, Y., Huang, A., & Zhu, X. (2006). Parameterization of the thermal impacts of sub-grid orography on numerical modeling of the surface energy budget over East Asia. *Theoretical and Applied Climatology*, *86*(1–4), 201–214. https://doi.org/10.1007/s00704-005-0209-1

Zhang, Y., Sieron, S. B., Lu, Y., Chen, X., Nystrom, R. G., Minamide, M., et al. (2021). Ensemble-based assimilation of satellite all-sky microwave radiances improves intensity and rainfall predictions for Hurricane Harvey (2017). *Geophysical Research Letters*, *48*(24), e2021GL096410. https://doi.org/10.1029/2021GL096410

Zhu, X., Duan, S. B., Li, Z. L., Zhao, W., Wu, H., Leng, P., et al. (2021). Retrieval of land surface temperature with topographic effect correction from landsat 8 thermal infrared data in mountainous areas. *IEEE Transactions on Geoscience and Remote Sensing*, *59*(59–8), 6674–6687. https://doi.org/10.1109/TGRS.2020.3030900

Zhuge, X., Zou, X., Weng, F., & Sun, M. (2018). Dependence of simulation biases at AHI surface-sensitive channels on land surface emissivity over China. *Journal of Atmospheric and Oceanic Technology*, *35*(6), 1283–1298. https://doi.org/10.1175/jtech-d-17-0152.1

Zou, X., Qin, Z., & Zheng, Y. (2015). Improved tropical storm forecasts with GOES-13/15 imager radiance assimilation and asymmetric vortex initialization in HWRF. *Monthly Weather Review*, *143*(7), 2485–2505. https://doi.org/10.1175/MWR-D-14-00223.1